ACS APPLIED ENERGY MATERIALS

www.acsaem.org

Article

Earth-Abundant Divalent Cation High-Entropy Spinel Ferrites as Bifunctional Electrocatalysts for Oxygen Evolution and Reduction Reactions

Tuncay Erdil, Cagla Ozgur, Uygar Geyikci, Ersu Lokcu, and Cigdem Toparli*

Cite This: ACS Appl. Energy Mater. 2024, 7, 7775−7786

Read Online

ACCESS | Metrics & More | Article Recommendations | Supporting Information

ABSTRACT: High-entropy spinel ferrites (HESFs) offer long-term stability and activity in oxygen electrochemical reactions due to entropy stabilization and synergistic effects of multiple elements within their crystal structure. However, conventional HESFs often rely on transition metals for high configurational entropy, limiting their accessibility and sustainability. In this study, we successfully synthesized a high-entropy spinel oxide using earth-abundant elements, such as Mg, Cu, and Zn (Mg-Fe_2O_4), addressing the need for more sustainable materials without compromising performance. Despite differences in cation composition, both synthesized HESFs maintain identical crystal structures and lattice constants. Incorporating smaller-radius elements like Mg, Cu, and Zn does not affect the crystal structure, achieving high-entropy spinel ferrites with similar properties to traditional counterparts, e.g., $(CoCrFeMnNi)Fe_2O_4$. Material characterization and electrochemical analyses demonstrate comparable performance, including over 200 h of continuous battery operation. These findings highlight the potential of utilizing more accessible materials to create efficient HESFs, expanding their applicability in energy conversion and storage.

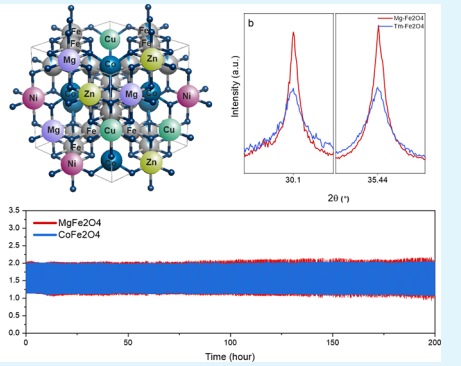

KEYWORDS: *high-entropy oxides, spinel ferrites, bifunctional electrocatalysis, zinc-air batteries, earth-abundant elements*

1. INTRODUCTION

High-entropy materials have emerged as an important point in materials science due to their unique, tailorable, and superior physicochemical properties.[1−3] These materials are distinguished by their remarkable crystal structure stability because of their high configurational entropy. The foundation of their entropically stabilized crystal structures lies in the incorporation of five or more cations within a single-phase crystal, distributed in equiatomic or near-equiatomic ratios.[4−6] This cationic diversity leads to an elevated configurational entropy (S_{config}), which has a significant negative contribution to overcome the enthalpy of mixing.[5] As a result, this high S_{config} exerts a significant negative impact, facilitating the achievement of a negative Gibbs free energy of formation, since the Gibbs equation is $\Delta G = \Delta H - T\Delta S$. This principle underscores the potential of high-entropy materials in overcoming traditional compositional limitations, offering a pathway to the development of materials with novel and enhanced functionalities. Achieving an S_{config} equal to or greater than 1.5R, where R is the universal gas constant, is a critical benchmark for the stabilization of high-entropy materials.[7,8] However, calculating S_{config} for oxide systems presents a more complex challenge than that for their metallic counterparts. This complexity arises due to the presence of multiple lattice sites within oxide crystal structures, necessitating the consideration of element distribution not only at cation sites but also at anion sites. Thus, to surpass the S_{config} threshold of 1.5R in oxides, it is essential to account for both cationic and anionic diversity.[5,9] Additionally, the metal/oxygen ratio becomes a crucial parameter influencing S_{config} values in oxides. A careful balance in this ratio can significantly impact the entropy contribution, thereby influencing the overall stability and properties of high-entropy oxides. This approach to entropy calculation underscores the multifaceted nature of designing high-entropy materials, particularly oxides, and highlights the importance of considering all compositional aspects to harness their full potential. High-entropy oxides (HEOs) possess distinct and tailorable material properties alongside exceptional structural stability; these make them promising candidates for electrocatalytic applications.[10,11] The synergistic effects arising from the coexistence of multiple elements at the same site within HEOs can profoundly alter their electronic structure, facilitating efficient charge carrier transport throughout the crystal lattice. HEOs include large numbers of different elements in their structures,

Received: May 15, 2024
Revised: August 22, 2024
Accepted: August 28, 2024
Published: September 10, 2024

creating a large number of available surface-active atomic sites and chemical environments for adsorption and activation of reactants.[12−14] These features make HEOs particularly well suited for applications in aqueous systems such as metal−air batteries.[15,16] By controlling these unique characteristics, HEOs hold great potential to enhance the performance and efficiency of electrochemical energy storage and conversion devices, offering a pathway toward sustainable and renewable energy technologies.[15−18] High-entropy alloys have attracted attention as stable electrocatalysts for the hydrogen evolution reaction (HER), while HEOs have demonstrated stability and efficiency as electrocatalysts for the oxygen evolution reaction (OER) and oxygen reduction reaction (ORR).[11,19,20] These reactions typically exhibit sluggish kinetics, posing challenges for maintaining stability with state-of-the-art electrocatalysts.[21] Ensuring stability, rapid kinetics, and conductivity is crucial for achieving cyclic stability and maintaining capacity, particularly in battery applications. Entropy stabilization plays a significant role in preserving capacity in HEO electrodes for both Li-ion and metal-air batteries, highlighting the importance of advantaging high-entropy materials for enhancing the performance and longevity of electrochemical energy storage systems.[22−25]

Spinel oxides, denoted by the general formula AB_2O_4, feature a distinctive crystal structure where A-ions are positioned in one-eighth of the tetrahedral sites and B-ions occupy half of the octahedral sites, resulting in a cubic close-packed structure. The composition and cation distribution within these oxides critically influence their magnetic, electronic, and optical properties, making them highly versatile across various applications.[26,27] Particularly for electrocatalyzing oxygen-related reactions, spinel oxides have demonstrated considerable potential, with many variants incorporating iron and cobalt at the B-site to enhance activity.[28−30] The ferrite ones have higher activities for OER such as $NiFe_2O_4$ and Tm-Fe_2O_4 showcasing enhanced OER activities.[31] This enhancement is often attributed to the synergistic interaction between Fe and other B-site cations like Ni, where iron not only acts as a structural enhancer but also significantly contributes to the electrocatalytic process.[32] Spinel ferrites, formulated as AFe_2O_4, can include a wide array of transition metals (e.g., Fe, Co, Cr, Mn, Ni) or divalent ions (Mg, Cu, Zn, etc.) at the A-site, offering a broad palette for tuning the material's properties to optimize for specific electrochemical reactions.[33,34] The spinel oxides can be in two forms: normal spinel and inverse spinel. In normal spinel, A elements only occupy tetrahedral sites, while in inverse spinel, they occupy both tetrahedral and octahedral sites. Spinel ferrites like Tm-Fe_2O_4,[17,18] $NiFe_2O_4$,[35,36] and $CoFe_2O_4$[33,37] have demonstrated efficient OER electrocatalytic performance, characterized by low overpotential values. This performance improvement often comes from the substitution of transition metal cations, which significantly alters the electronic structure of the material. Multimetallic oxides generally outperform single-metal oxide catalysts due to their lower activation energies for interatomic charge transfer. Hence, engineering spinel ferrites with diverse valence oxides allows for the adjustment of their electronic structure, consequently enhancing intrinsic properties, such as conductivity. Additionally, cation substitution with varying ionic radii can induce structural distortions, altering the lattice parameters, atomic positions, and electronic structure. Moreover, the stability and activity of the OER in spinel ferrites are influenced by entropy-induced structural stability. High-entropy spinel ferrites (HESFs) have recently garnered attention for various applications, including photoelectrochemical water splitting,[17] sulfur host materials for lithium-sulfur batteries,[22,38] Li-ion batteries,[24,25,39] catalytic activation of peroxodisulfate,[40] magnetic insulation,[41] microwave absorption,[42] and oxygen evolution catalysts.[17,18,28,30] This broad applicability underscores the versatility and potential of HESFs in the diverse fields of material science and energy conversion technologies.

In most of the HEOs and HESFs, transition metals are used to achieve high configurational entropy to produce the high-entropy oxide, but in this study, we successfully synthesized a high-entropy spinel oxide with earth-abundant elements such as Mg, Cu, and Zn. In this study, we successfully synthesized two variants of high-entropy cubic spinel ferrites with identical lattice properties but distinct cation compositions at the A-site. One variant includes a traditional mix of transition metals (Fe, Co, Cr, Mn, Ni) at the A-site, $(CoCrFeMnNi)Fe_2O_4$ denoted as Tm-Fe_2O_4, while the other consists of earth-abundant elements (Mg, Cu, Zn) in addition to Co and Ni, i.e., $(MgCoCuNiZn)Fe_2O_4$ denoted as Mg-Fe_2O_4. This innovative approach addresses the need for more sustainable and accessible materials without compromising the structural integrity or electrocatalytic performance of the HESFs. Both synthesized HESFs, despite their differing cation compositions, maintain the same crystal structure, characterized by a very similar lattice constant. The incorporation of smaller-radius elements such as Mg, Cu, and Zn into the ferrite spinel structure does not induce lattice strain nor alter the crystal structure, thereby achieving a high-entropy spinel ferrite with an identical configurational enthalpy and lattice constant compared to traditional HESFs. Furthermore, the oxidation states of all common elements in both HESF types remain consistent. Material characterization and electrochemical analyses reveal that the earth-abundant element-based HESFs not only mirror the crystal and electronic structure of their transition-metal-only counterparts but also perform comparably as electrocatalysts. This finding underscores the potential of utilizing more readily available materials to create efficient, high-performing HESFs, thereby broadening the accessibility and sustainability of high-entropy materials for various applications, particularly in the fields of energy conversion and storage.

2. EXPERIMENTAL SECTION

2.1. Synthesis of High-Entropy Spinel Ferrites. In this study, two high-entropy spinel ferrites (HESFs), namely, $(MgCoCuNiZn)Fe_2O_4$ (Mg-Fe_2O_4) and $(CoCrFeMnNi)Fe_2O_4$ (Tm-Fe_2O_4), were synthesized using the facile sol−gel Pechini method, which is detailed in our previous works. The synthesis started with the dissolution of stoichiometric amounts of metal nitrate salts into deionized (DI) water. This dissolution process was carried out under continuous stirring at a temperature of 100 °C to ensure complete solubilization of the salts. Following the dissolution, citric acid and acrylamide were added into the solution as chelating agents. These were added in a specific molar ratio of metal nitrates to citric acid to acrylamide, which was maintained at 1:9:3, respectively. This ratio was carefully chosen to ensure the optimal chelation of metal ions, thereby facilitating the formation of a homogeneous gel, which is a precursor to the high-entropy spinel ferrite phase. Subsequent to drying, the gel underwent a two-stage heat treatment process. Initially, the dried gel was calcinated at a temperature of 600 °C. Following calcination, the material was further annealed at a temperature of 900 °C. This annealing step is essential for achieving a single-phase material with a well-defined crystalline structure. Lastly, to ensure uniform particle

https://doi.org/10.1021/acsaem.4c01227
ACS Appl. Energy Mater. 2024, 7, 7775−7786

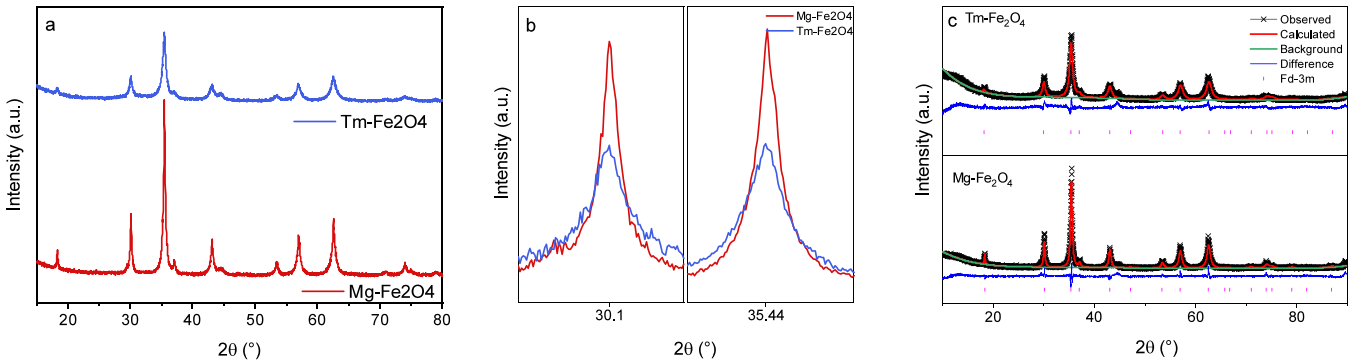

Figure 1. (a) XRD patterns of HESFs. (b) Main XRD peaks of Mg-Fe_2O_4 and Tm-Fe_2O_4 at 30.1 and 35.44°. (c) Rietveld refinement analysis for Tm-Fe_2O_4 and Mg-Fe_2O_4.

size and to enhance the homogeneity of the synthesized powders, the obtained single-phase materials were subjected to ball milling. This process was conducted for a duration of 12 h at a rotational speed of 400 rpm.

2.2. Material Characterization. The crystalline structure of the synthesized specimens was examined through powder X-ray diffraction (XRD) analysis conducted at room temperature, employing Ni-filtered Cu Kα radiation (λ = 1.5406 Å); diffraction patterns were collected over a 2θ range of 10−80°. To ascertain the phase purity and refine the crystallographic data of the specimens, the Rietveld refinement method was utilized by using the GSAS II software package. The detailed morphological study and selected area electron diffraction (SAED) patterns of the HESFs were conducted using a field-emission high-resolution transmission electron microscope (HRTEM, Tecnai G2 F30). The chemical composition and electronic state of elements within the HESFs were characterized using X-ray photoelectron spectroscopy (XPS). Analysis was carried out on a PHI 5000 Versa Probe spectrometer, utilizing Al Kα radiation as the excitation source. To ensure accuracy in the measurement, all spectral peaks were calibrated against the standard carbon 1s peak at 284.8 eV, providing a reference for the binding energy scale. Ultraviolet photoelectron spectroscopy (UPS) experiments were conducted to investigate the surface electronic structure and calculate the work function of the HESFs. These experiments were performed using a Physical Electronics (PHI) Versa Probe 5000 under high vacuum conditions (base pressure of 1×10^{-9} mbar). A He gas discharge lamp emitting at 21.22 eV served as the UV light source. The work function values were determined by subtracting the He I radiation energy from the high-binding-energy cutoff observed in the UPS spectra. To ensure the reliability of the energy measurements, Fermi edge calibration was executed by using a sputter-cleaned silver (Ag) standard, aligning all energies with a common Fermi level (0 eV).

2.3. Electrochemical Measurements. The electrocatalytic performance of the Mg-Fe_2O_4 and Tm-Fe_2O_4 high-entropy spinel ferrites (HESFs) toward the OER and ORR was assessed using a rotating disc electrode (RDE, BASI) system interfaced with a GAMRY Reference 3000 potentiostat/galvanostat. These investigations were carried out in a standard three-electrode configuration, comprising a glassy carbon electrode (GCE) as the working electrode, a platinum wire was used as the counter electrode for the OER, a graphite counter electrode was used for collecting ORR data, and an Ag/AgCl electrode was used as the reference, in an oxygen-saturated 0.1 M KOH aqueous electrolyte. A catalyst ink was prepared by mixing 5 mg of Super-P carbon black and 10 mg of the HESF powder with 200 μL of a 5 wt% Nafion solution and 2 mL of ethanol. This homogeneous mixture was sonicated to ensure uniform dispersion. Subsequently, 10 μL of this catalyst ink was drop-casted onto the GCE, achieving a catalyst loading of approximately 0.557 mg_{HESF} cm_{disk}^{-2}. Prior to each set of measurements, the HESF-coated electrodes were electrochemically conditioned through a sequence of 10 cyclic voltammetry (CV) sweeps within a potential range specific to the OER (0.2 to 1.1 V vs Ag/AgCl) and ORR (0.2 to −1.1 V vs Ag/AgCl) to activate the catalyst surface. During these procedures, a constant flow of oxygen was maintained in the electrolyte and the RDE was operated at 1600 rpm. Linear sweep voltammetry (LSV) tests, with a scan rate of 10 mV/s, spanned from 0.2 to 1.1 V vs Ag/AgCl for the OER activity evaluation. The obtained potentials were *iR*-corrected and recalibrated to the reversible hydrogen electrode (RHE) scale via the given Nernst Equation for pH 12.6 (specific to 0.1 M KOH): $E_{vsRHE} = E_{vsAg/AgCl} + 0.059 \times pH + 0.1976$ pH. Tafel slopes were extracted by plotting the potential against the logarithm of the current density from the polarization curves. Electrochemical impedance spectroscopy (EIS) measurements were conducted at an applied potential of 0.7 V vs Ag/AgCl, over a frequency range of 10^5 to 10^{-2} Hz, with an amplitude of 10 mV AC voltage. The electrochemically active surface area (ECSA) of the HESF electrocatalysts involved the utilization of double-layer capacitance (C_{dl}), derived from CV analyses at various scan rates (20, 40, 60, 80, 100, and 120 mV s^{-1}) within the nonfaradaic region, i.e., 0.2−0.3 V vs Ag/AgCl. A graph depicting the scan rate against the reciprocal of the difference between anodic and cathodic current densities ($\Delta J/2 = (J_a - J_c)/2$) was then constructed at 0.25 V vs Ag/AgCl. Subsequent linear fitting enabled the determination of C_{dl} for the NBCF electrocatalysts, employing half of the slope. ECSA was subsequently computed by dividing C_{dl} by the specific capacitance (C_s), equal to 0.040 mF.cm^{-2} in 1 M KOH according to the literature. For ORR, the identical experimental protocols were followed, modifying only the potential window to 0.2 to −1.1 V vs Ag/AgCl. The kinetic current density and the electron transfer number for the HESF catalysts during ORR were derived from the Koutecky−Levich (K−L) equation, based on LSV tests conducted at different rotation speeds (from 400 to 2000 rpm) and a scan rate of 5 mV s^{-1}, in the potential range of 0.2 to −0.8 V vs Ag/AgCl.

2.4. Measurement of the Zinc-Air Battery Performance. Zinc-air batteries (ZABs) were constructed using a custom-designed battery cell configuration comprising a bare zinc plate as the anode, a carbon cloth air cathode coated with HESF electrocatalysts, and a 6 M KOH electrolyte with 0.2 M $Zn(OAc)_2$ additive. The carbon cloth air cathode facilitated the entering of oxygen from the surroundings into the cell while preventing electrolyte leakage. The power densities of the HESF-based ZABs were evaluated by scanning the current density from 0 to 200 mA cm^{-2}, accompanied by the generation of charge and discharge polarization curves. Subsequently, the cyclic charge−discharge stability of the HESF-based ZABs was investigated at a constant current density of 5 mA cm^{-2}. During this evaluation, the batteries were subjected to successive charge and discharge cycles, each lasting 5 min.

3. RESULTS AND DISCUSSION

3.1. Crystal Structure and Electronic Structure Characterization. High-entropy oxides are favored as electrocatalysts due to their entropy stabilization mechanism,

https://doi.org/10.1021/acsaem.4c01227
ACS Appl. Energy Mater. 2024, 7, 7775−7786

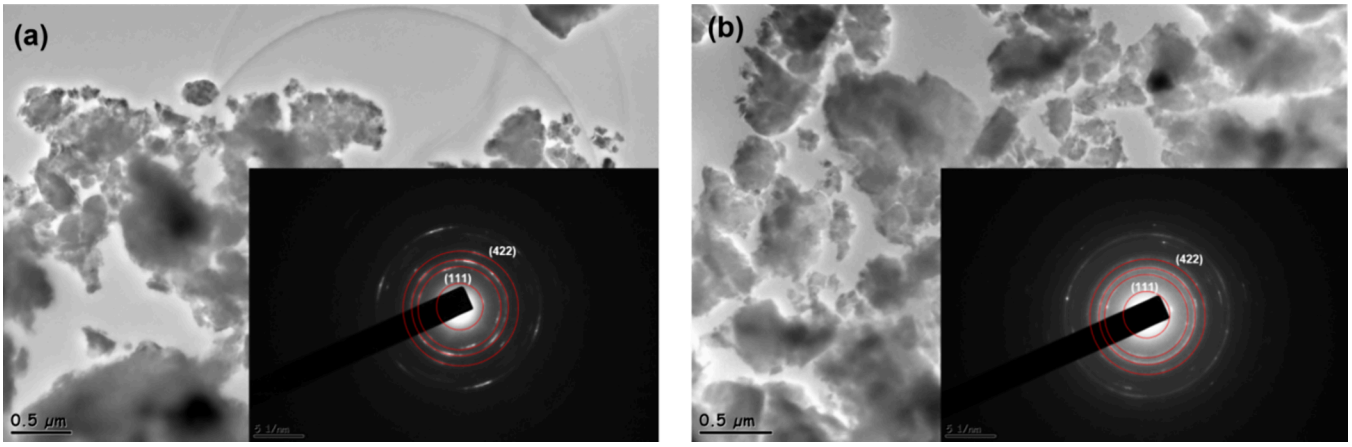

Figure 2. TEM images and corresponding SAED patterns (inset) of (a) Mg-Fe_2O_4 and (b) Tm-Fe_2O_4.

which enhances the stability of their single-phase crystal structure. This stabilization is achieved by increasing the S_{config} value within the lattice sites, which occurs when the constituent elements are randomly distributed. As a result, HEOs exhibit remarkable structural stability, making them promising candidates for various electrocatalytic applications. The S_{config} for oxide systems can be calculated using the equation below.[5,9]

$$S_{config} = -R\left[\left(\sum_{i=1}^{n} x_i \ln x_i\right)_{cation-site} + \left(\sum_{j=1}^{n} x_j \ln x_j\right)_{anion-site}\right]$$

where x_i and x_j represent the mole fractions of the elements present in the cation and anion sites and R is the universal gas constant. The materials can be classified as follows related to their configurational entropies empirically: materials with $S_{config} > 1.5R$ are high-entropy materials, with $R < S_{config} < 1.5R$ being medium-entropy materials and those with $S_{config} < R$ being low-entropy materials. Since the mole fractions are the same for both Mg-Fe_2O_4 and Tm-Fe_2O_4, their configurational entropies are also the same. Since the only A-site of the high-entropy spinel ferrite occupied more than one element, the S_{config} value is 1.6094R for both Mg-Fe_2O_4 and Tm-Fe_2O_4.

Figure 1a displays the XRD patterns of single-phase cubic spinel ferrites without any impurity phases. Both HESFs exhibit identical crystal structures, indicating the feasibility of synthesizing HESFs with similar lattice constants by altering the elemental compositions. The main peak positions in Figure 1b prove the same crystal structure without any lattice strain. Rietveld refinement in Figure 1c confirms the cubic crystal structure (space group: $Fd\bar{3}m$) with lattice constants of 8.353 Å for Tm-Fe_2O_4 and 8.352 Å for Mg-Fe_2O_4. Both HESFs adopt an inverse spinel structure, where transition metals occupy both tetrahedral and octahedral sites due to their 2+ and 3+ charge states. This structural arrangement is explained further in the XPS section. The XRD refinement indicates the potential to synthesize high-entropy spinel oxides with identical crystal structures using cost-effective and abundantly available elements such as Mg, Cu, and Zn.

TEM analysis was conducted to examine the morphologies of the powders and to understand the similar crystal structures of HESFs. Figure 2 depicts TEM images of HESFs, revealing consistent particle sizes and morphologies. Both powders exhibit uniform particle dimensions ranging from 500 to 600 nm, attributable to the synthesis method and ball milling process. The SAED patterns of both HESFs are very similar to each other as expected from the XRD patterns. The inset of Figure 2a shows the SAED pattern of the Tm-Fe_2O_4, and the inset of Figure 2b shows the Mg-Fe_2O_4. The rings correspond to (111), (311), (400), and (422) planes, respectively. As shown in these figures, both HESFs have very similar d-spacing values; this indicates their very similar lattice constants.

The chemical composition and the oxidation states of the HESFs are investigated by XPS. The Fe 2p spectra of Mg-Fe_2O_4 and Tm-Fe_2O_4 in Figure 3a exhibit the peaks at 710.7 and 710.9 eV ($2p_{3/2}$) and 724.4 and 724.6 eV ($2p_{1/2}$) and the spin−orbital at 13.7 eV, respectively. Satellites were observed between 714 and 720 eV and 730−735 eV; these features indicate the presence of 2+ and 3+ of the iron oxidation states.[43,44] This implies that iron occupies both tetrahedral and octahedral sites in the crystallographic structure. The Co 2p XPS spectra exhibit peaks at 781.3 eV for $Co2p_{3/2}$ and 795.4 eV for $Co2p_{1/2}$ with the satellite peaks around 787 and 805 eV; both HESFs suggest the valence state of Co^{2+} and Co^{3+} (Figure 3B).[45] It is hard to identify the $Co2p_{3/2}$ peak because this peak overlaps with the Fe and Ni LMM Auger peaks, which are at the binding energies at 784 and 778 eV, respectively, which causes a superposition of the Co main peak.

The XPS spectra of Ni 2p as shown in Figure 3c have two main peaks at 854.9 and 873.4 eV, and these peaks correspond to $Ni2p_{3/2}$ and $Ni2p_{1/2}$, respectively. There are two satellite peaks around 860 and 880 eV, stating the presence of Ni^{2+} and Ni^{3+}, respectively.[46,47] The Cu 2p peaks for $Cu2p_{3/2}$ and $Cu2p_{1/2}$ are positioned at 932.3 and 952.5 eV, respectively, as shown in Figure 3d. The main peaks and the satellite peaks of Cu 2p indicate that Cu only has a Cu^{2+} oxidation state; thus, it is probably located at the tetrahedral site of the spinel structures.[48] Zn 2p does not show any satellite peak Zn expected to be only 2+ charge, so that it occupies at the tetrahedral site (Figure 3e).[17] The Mg 2p spectra only show one main peak at 55.1 eV, and due to the very small spin−orbit splitting, Mg only has 2+ charge and occupies only in the tetrahedral site like Zn, as shown in Figure 3f.[17] The 2p signals of the metals of both HESFs have the same binding energies and oxidation states. This implies that it is possible to synthesize a high-entropy spinel oxide with a high configuration entropy using cheaper and more abundant elements like Mg, Cu, and Zn. Figure 3g,h shows that the O 1s XPS spectra of HESFs can be deconvoluted into four peaks, which

https://doi.org/10.1021/acsaem.4c01227
ACS Appl. Energy Mater. 2024, 7, 7775−7786

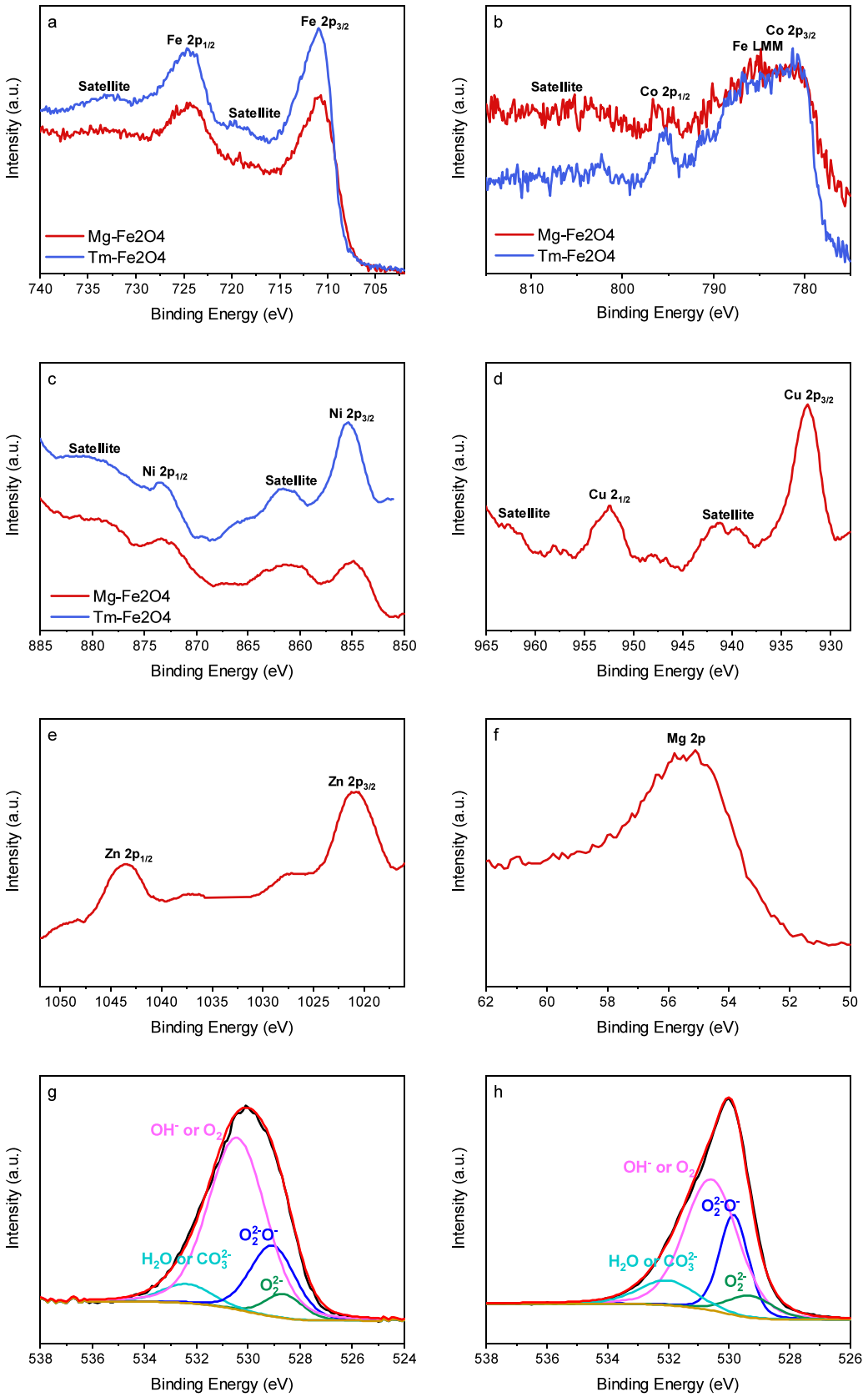

Figure 3. XPS core-level spectra of (a) Fe 2p, (b) Co 2p, and (c) Ni 2p for Mg-Fe_2O_4 and Tm-Fe_2O_4. XPS core-level spectra of Mg-Fe_2O_4 for (d) Cu 2p, (e) Zn 2p, and (f) Mg 2p and deconvoluted O 1s spectra of (g) Mg-Fe_2O_4 and (h) Tm-Fe_2O_4.

correspond to lattice oxygen species, i.e., first two peaks, and oxygen vacancy species, i.e., peaks with higher eVs. The first peak around 528 eV corresponds to the lattice oxygen species, showing the presence of the O^{2-} ions within the lattice. The

https://doi.org/10.1021/acsaem.4c01227
ACS Appl. Energy Mater. 2024, 7, 7775−7786

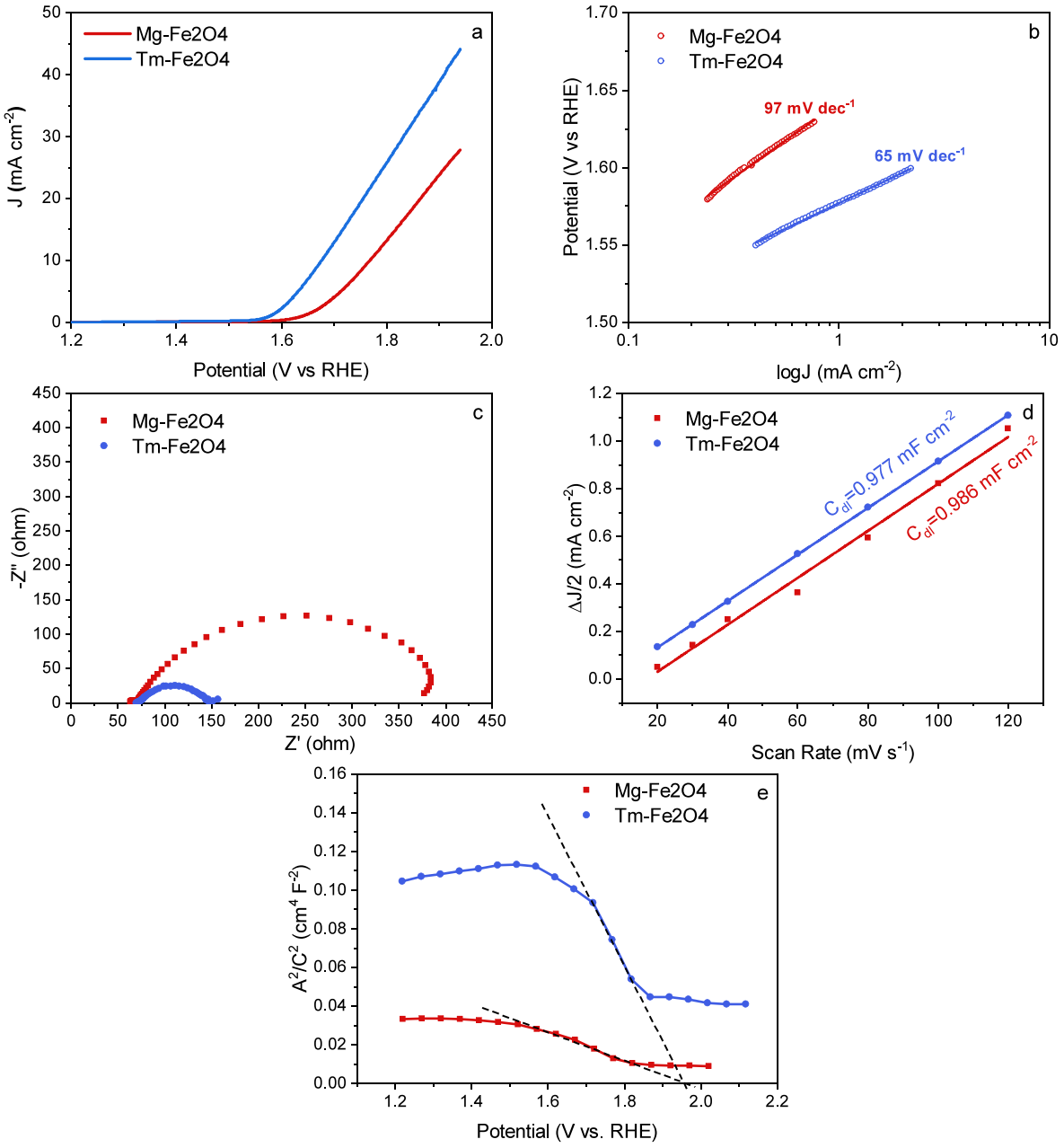

Figure 4. (a) LSV curves for the OER activity. (b) Corresponding Tafel slopes. (c) Electrochemical impedance spectroscopy curves. (d) Electric double-layer capacitance. (e) Mott−Schottky plots for Mg-Fe_2O_4 and Tm-Fe_2O_4.

second peak near 529 eV is situated in the O_2^{2-}/O^- highly oxidative oxygen species. The following peaks around 531 and 532 eV correspond to the oxygen vacancies such as OH^-/O_2 and molecular water or surface-bound carbonates, respectively.[49,50] The oxygen vacancies have a great impact on the electrocatalytic performance of the electrocatalysts. However, the oxygen vacancies and OH^- peaks are similar for both Mg-Fe_2O_4 and Tm-Fe_2O_4.

The spinel can be in the form of normal spinel and inverse spinel. The normal spinel structure positions divalent cations in tetrahedral sites, while trivalent cations occupy octahedral sites. Conversely, the inverse spinel structure features both divalent and trivalent cations distributed across both tetrahedral and octahedral sites. In the specific case of Mg-Fe_2O_4, divalent elements such as Mg, Cu, and Zn exclusively take place in tetrahedral sites due to their consistent 2+ oxidation state. Conversely, Fe, Co, and Ni, which can exist in both 2+ and 3+ oxidation states, are located across both tetrahedral and octahedral sites, displaying versatile occupancy patterns dictated by their variable valence states.

3.2. Electrochemical Performance of the Electrocatalysts. The electrocatalytic efficacy of HESFs was examined using a standard three-electrode setup in an RDE configuration for precision analysis of the OER. Electrochemical experiments employed a Ag/AgCl reference electrode, with all measured potentials recalibrated to the RHE scale for standardized comparison. The evaluated current densities were normalized to the surface area of the utilized GCE, specifically 0.0707 cm^2. Experimental findings revealed a distinguishable variance in overpotential values between the two HESFs; Tm-Fe_2O_4 exhibited an overpotential of 446 mV, whereas Mg-Fe_2O_4 demonstrated a higher overpotential of 539

https://doi.org/10.1021/acsaem.4c01227
ACS Appl. Energy Mater. 2024, 7, 7775−7786

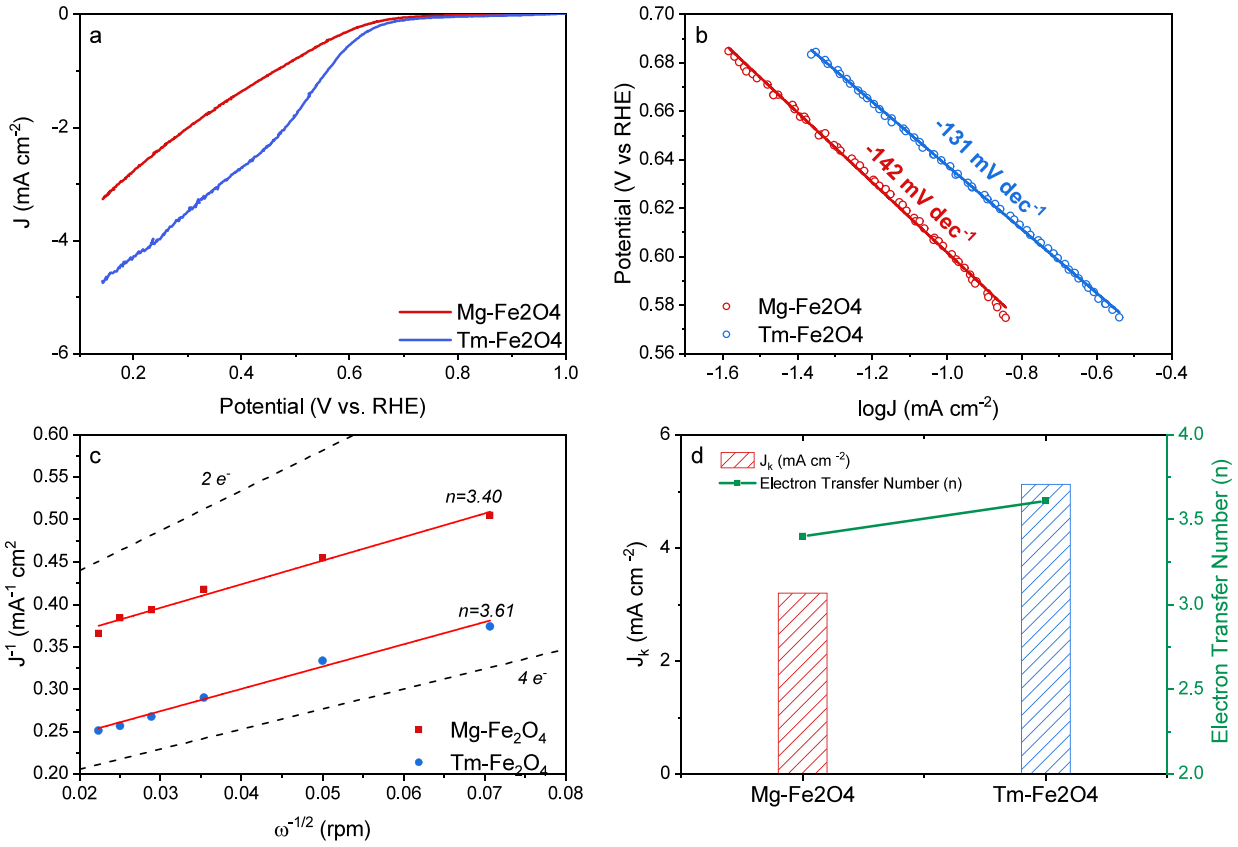

Figure 5. (a) LSV curves for ORR activity. (b) Corresponding Tafel slopes. (c) Koutecky–Levich plots. (d) Electron transfer number (n) and kinetic current density (J_k) for Mg-Fe_2O_4 and Tm-Fe_2O_4.

mV at a benchmark current density of 10 mA cm^{-2} in 0.1 M KOH, as shown in Figure 4a. This observed difference underscores the significant role of transition metal elements (e.g., Co, Fe, Cr, and Mn) present in the A-site of the spinel structure, influencing the electrocatalytic performance and OER efficiency, thereby highlighting the impact of transition metal cations on facilitating lower energy barriers for electrochemical reactions.

The kinetic characteristics of the HESFs as electrocatalysts were quantitatively assessed through Tafel analysis, facilitating a deeper understanding of the mechanisms of the OER, as depicted in Figure 4b. Tafel slopes, pivotal for evaluating reaction kinetics, revealed distinctions between the electrocatalysts. Tm-Fe_2O_4 demonstrated a Tafel slope of 65 mV dec^{-1}, indicating more favorable reaction kinetics, whereas Mg-Fe_2O_4 exhibited a steeper slope of 97 mV dec^{-1}. This differential suggests that Tm-Fe_2O_4 facilitates a more rapid electrochemical reaction, attributable to its lower Tafel slope, thereby denoting faster electron transfer processes and enhanced catalytic efficiency during the OER. Interestingly, despite the absence of transition metals within its structure, Mg-Fe_2O_4 still presents a comparable overpotential and kinetic profile for the OER with Tm-Fe_2O_4, highlighting its potential utility in electrocatalytic applications.

Electrochemical impedance spectroscopy (EIS), illustrated in Figure 4c, provides valuable insights into the charge transfer dynamics of the electrocatalysts during the operation. The EIS data are fitted to a model comprising solution resistance (R_s), a constant phase element (CPE), and the charge transfer resistance (R_{ct}). Tm-Fe_2O_4 exhibits a charge transfer resistance of 80 ohms, significantly lower than the 300 ohms recorded for Mg-Fe_2O_4. This contrast implies the superior charge transfer kinetics and enhanced conductivity of Tm-Fe_2O_4 relative to Mg-Fe_2O_4. The observed difference in charge transfer resistance aligns with the superior OER performance of Tm-Fe_2O_4, highlighting the critical role of conductivity and charge transfer kinetics in electrocatalytic efficiency.

Additionally, the ECSA of the HESF electrocatalysts was assessed through the measurement of double-layer capacitance (C_{dl}), as depicted in Figure 4d. The calculated C_{dl} values for Mg-Fe_2O_4 and Tm-Fe_2O_4 were determined as 9.86 and 9.77 mF cm^{-2}, respectively. This analysis reveals that both HESFs possess nearly identical active surface areas in terms of ECSA, indicating their comparable electrochemical reactivity. The ECSA exhibits a strong correlation with other electrochemical measurements, further validating the comprehensive characterization and performance evaluation of the HESF electrocatalysts.

The Mott–Schottky (MS) analysis in Figure 4e provides crucial insights into the semiconducting properties of electrocatalysts, which are essential for understanding their electrochemical reaction mechanisms.[S1,S2] The observed p-type behavior for both HESF electrocatalysts throughout and beyond the OER potential regime (around 1.23 V vs RHE) suggests that the majority carriers are holes. The lack of a transition from n-type to p-type semiconductor behavior between 1.2 and 2 V indicates a stable p-type conductivity within this potential range, which is significant for OER applications. The similarity in flat-band potential (E_{fb}) between Mg-Fe_2O_4 and Tm-Fe_2O_4 further indicates the similar intrinsic semiconductor characteristics of these electrocatalysts despite their distinct elemental compositions. This finding is in line

https://doi.org/10.1021/acsaem.4c01227
ACS Appl. Energy Mater. 2024, 7, 7775–7786

with their crystal structure, oxidation states, and semiconductor behavior, suggesting that the high-entropy approach allows for the tuning of elemental composition without drastically altering key material properties critical for electrocatalysis. Such intrinsic semiconductor behavior is crucial for understanding how these materials facilitate charge transfer processes during the OER. In p-type semiconductors, the proximity of the flat-band potential to the OER potential can influence the ease with which holes are generated and participate in the water oxidation process. The fact that both HESFs demonstrate similar intrinsic semiconductor behavior implies that the unique combination of elements in high-entropy configurations does not compromise their fundamental electronic properties, which are critical for an efficient and stable OER performance.

The ORR performances of both HESFs were thoroughly examined to understand their catalytic efficiency. Since the Pt clusters can be deposited onto the surface of the working electrode, a graphite counter electrode was used in the ORR measurement to eliminate the performance increase with Pt deposition. The onset potentials, determined at −1 mA cm^{-2} from the LSV curves in Figure 5a, revealed a little difference between the two electrocatalysts. Tm-Fe_2O_4 exhibited an onset potential of 0.557 V, whereas Mg-Fe_2O_4 displayed a slightly lower onset potential of 0.467 V. This discrepancy indicates a variation in the ORR activity between the two materials. Tafel slope analysis was conducted to understand the kinetics of the ORR (Figure 5b. The Tafel slopes were calculated as −131 mV dec^{-1} for Tm-Fe_2O_4 and −142 mV dec^{-1} for Mg-Fe_2O_4, suggesting faster reaction kinetics for Tm-Fe_2O_4 compared to Mg-Fe_2O_4.

Further insight into the electron transfer mechanism was obtained through Koutecky−Levich (K−L) analysis, as depicted in Figure 5c, which allows for the determination of electron transfer number (n) and kinetic current densities. K−L plots were generated from the LSV curves over a range of rotational speeds (400, 800, 1200, 1600, and 2000 rpm) and a scan rate of 5 mV s^{-1}, revealing a linear relationship indicative of first-order kinetics for both HESFs. The rotational speed of the working electrode affects the reduction current. When the rotational speed increases, the mass transport at the working electrode surface improves, so that the reduction current increases. Also, the increase in the rotational speed causes enhancement of the diffusion of the oxygen in the electrolyte to the surface of the electrocatalysts. Notably, Tm-Fe_2O_4 exhibited a higher reduction current density at constant potential and rotational speed compared to Mg-Fe_2O_4. The electron transfer number (n) at 0.25 V vs RHE was determined to be 3.61 for Tm-Fe_2O_4 and 3.40 for Mg-Fe_2O_4, further confirming their distinct catalytic behaviors (Figure 5d). Overall, these findings shed light on the electrochemical behavior of HESF electrocatalysts for the ORR. The distinct performance characteristics observed between Tm-Fe_2O_4 and Mg-Fe_2O_4 indicate the importance of understanding the catalyst's composition and structural properties in tailoring their catalytic activity. The electron transfer number was calculated from the K−L equation given below:

$$\frac{1}{J} = \frac{1}{J_k} + \frac{1}{n \times B\omega^{0.5}}$$

where J_k is the kinetic current density, n is the kinetic current density, n is the electron transfer number, w is the rotation speed, and B is the Levich constant, which is $B = (0.620)FAD_{O2}{}^{2/3}\nu^{-1/6}C_{O2}$ = constant, where F is the Faraday constant, A is the electrode area, D_{O2} is the oxygen diffusion coefficient, v is the kinematic viscosity, and C_{O2} is the oxygen concentration. The observation that both HESFs, Tm-Fe_2O_4 and Mg-Fe_2O_4, exhibit electron transfer numbers close to 4 highlights the prevalence of the four-electron ORR pathway in these materials. This is significant since the four-electron pathway is more desirable for applications than the two-electron pathway, as it leads directly to water without the formation of hydrogen peroxide intermediate, thereby achieving higher energy efficiency and reduced oxidative stress. The reaction kinetics values, determined to be 5.12 for Tm-Fe_2O_4 and 3.20 for Mg-Fe_2O_4, indicate the speed at which the ORR occurs on the electrocatalyst's surface. These values, in combination with the close electron transfer numbers for both HESFs, suggest that despite the differences in their elemental compositions, both Tm-Fe_2O_4 and Mg-Fe_2O_4 facilitate the ORR predominantly through the four-electron process and low kinetic current densities.[53]

The bifunctional index (BI) offers a comprehensive measure of an electrocatalyst's performance for both the OER and the ORR in a single metric. It quantifies the potential gap between the onset potential for ORR (measured at −1 mA cm^{-2}) and the potential required to achieve a current density of 10 mA cm^{-2} for the OER. A lower BI indicates a smaller potential gap and thus a higher efficiency of the electrocatalyst for both reactions, making it a crucial parameter for evaluating materials for applications such as rechargeable metal-air batteries and regenerative fuel cells. The reported BI values for Tm-Fe_2O_4 (1.12 V) and Mg-Fe_2O_4 (1.30 V) indicate that Tm-Fe_2O_4 possesses a narrower potential gap between its OER and ORR activities compared to Mg-Fe_2O_4, underscoring its superior bifunctional electrocatalytic performance in alkaline media. This suggests that Tm-Fe_2O_4 is more efficient in catalyzing both the reactions with less energy loss, making it a more suitable candidate for energy conversion and storage applications. However, the bifunctional performance of Mg-Fe_2O_4 cannot be ignored; it is still effective for oxygen electrochemical reactions. The closer BI value for Tm-Fe_2O_4 can be attributed to its material characteristics, such as the presence of transition metals at the A-site, which have been shown to enhance electrocatalytic activity due to their favorable electronic structures and oxidation states. Despite the similar physical and electronic properties exhibited by both HESFs, as indicated by their crystal structures, ECSAs, and intrinsic semiconductor behaviors, the presence of transition metals in Tm-Fe_2O_4 likely contributes to its enhanced electrocatalytic performance. While the difference in BI between Tm-Fe_2O_4 and Mg-Fe_2O_4 is not highly distinctive, it is still significant enough to impact their suitability for specific electrocatalytic applications. Enhancing the performance of Mg-Fe_2O_4 could involve strategies aimed at reducing its BI, such as optimizing the material's electronic structure or surface properties to improve its ORR and OER activities.

3.3. Analysis of the Electronic Structure. The work function of a material plays a crucial role in dictating its performance in oxygen electrochemical reactions, including the OER and the ORR. In HESF electrocatalysts, the work function is a key parameter that influences their catalytic activity and efficiency in these reactions. The work function of HESFs was experimentally determined using UPS, employing a bias voltage of −7 eV. The UPS work function spectra,

https://doi.org/10.1021/acsaem.4c01227
ACS Appl. Energy Mater. 2024, 7, 7775−7786

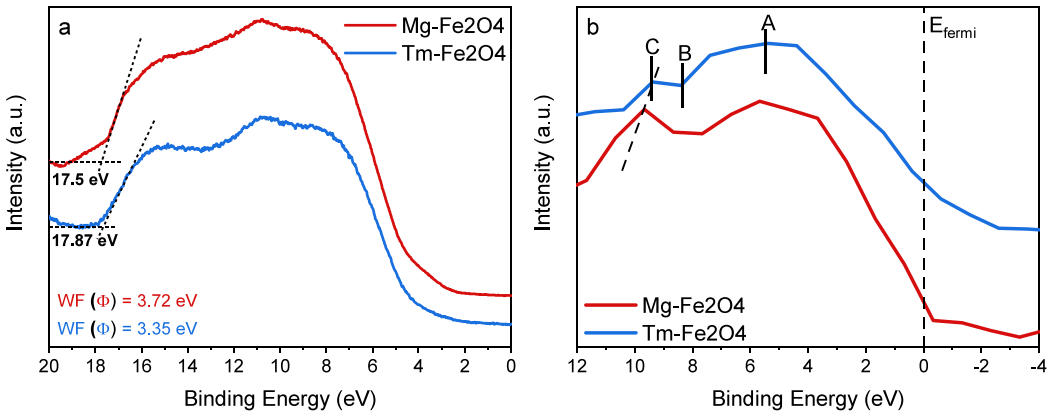

Figure 6. (a) UPS spectra and (b) XPS valence band spectra of Mg-Fe_2O_4 and Tm-Fe_2O_4.

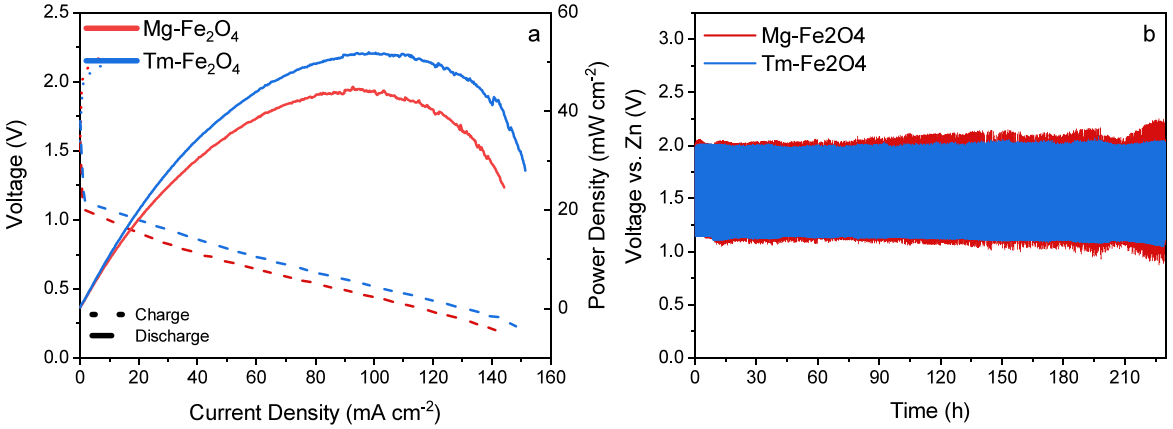

Figure 7. ZAB performance with HESFs based air cathodes. (a) Power density plots with charge and discharge polarization curves. (b) Cyclic charge−discharge performances at 5 mA cm^{-2}.

depicted in Figure 6a, were obtained by subtracting the energy of He (I) radiation (21.22 eV) from the high-binding energy cutoff. Additionally, Fermi edge calibration was conducted by using a sputter-cleaned Ag standard, ensuring that all energy measurements were referenced to a common Fermi level (0 eV). The UPS analysis provides valuable insights into the electronic structure of HESFs, specifically their work function, which directly influences their interaction with oxygen species during electrochemical reactions. The work function was calculated using the following equation:

$$\phi = h\nu - (E_{\text{cuttoff}} - E_{\text{Fermi}})$$

where $h\nu$ is the incident photoelectron energy (21.22 eV); E_{cutoff} was determined from the linear extrapolation with the baseline of the secondary electron onset. The work function of Tm-Fe_2O_4 is measured at 3.35 eV, while that of Mg-Fe_2O_4 is slightly higher at 3.72 eV. This disparity suggests that Tm-Fe_2O_4 possesses a higher intrinsic conductivity compared with Mg-Fe_2O_4, a finding that aligns with the EIS results. Despite the lower work function of Mg-Fe_2O_4, it remains a promising candidate for bifunctional electrocatalysis in oxygen evolution and reduction reactions. The work function values provide crucial insights into the electronic properties of HESF electrocatalysts, influencing their interaction with oxygen species during catalytic reactions. Despite differences in work function, both Tm-Fe_2O_4 and Mg-Fe_2O_4 exhibit the potential for efficient oxygen electrochemical reactions. The valence band (VB) spectra depicted in Figure 6b illustrates the hybridization of O 2p electronic states with transition metal 3d states in both HESFs. This hybridization pattern highlights the intricate electronic interactions within the HESF structures, which play a crucial role in their electrocatalytic performance. By characterizing the positioning of the O 2p-band center in relation to the Fermi energy, these spectra provide valuable insights into the electronic structure of the HESF electrocatalysts.

The XPS valence band spectra validation that both HESFs exhibit the synergistic hybridization of the O 2p and transition metal 3d orbitals is a significant insight into their electrocatalytic mechanism. This hybridization narrows the charge transfer gap at the electrocatalysts' surface, enabling a more efficient interaction with oxygen intermediate species in alkaline electrolytes. This interaction is crucial for facilitating the exchange of O_2^{2-}/OH^- on the surface, which is essential for the regeneration of OH^- during OER and ORR.[48] The successful synthesis of HESFs using cost-effective and abundant elements like Mg, Cu, and Zn without compromising the structural and electrochemical properties typically associated with more expensive materials is a commendable achievement. The fact that Mg-Fe_2O_4 displays characteristics remarkably similar to those of Tm-Fe_2O_4, including identical crystal structures, very similar lattice constants, the same oxidation states for their transition metals, low work functions, and evidence of O 2p hybridization, indicates the potential of utilizing these materials in energy-related applications. These findings signify the promise of HESFs, especially those

https://doi.org/10.1021/acsaem.4c01227
ACS Appl. Energy Mater. 2024, 7, 7775−7786

incorporating cheap and abundant elements, as efficient bifunctional electrocatalysts for oxygen electrochemical reactions. Their low work function values and the beneficial hybridization between O 2p and transition metal 3d states contribute to their high activity. This opens up new paths for the development of cost-effective, efficient, and durable materials for electrochemical energy conversion and storage technologies, potentially making sustainable energy systems more accessible.

3.4. Zinc-Air Battery Performance. The efficacy of high-entropy spinel ferrite electrocatalysts was evaluated using a homemade zinc-air battery configuration. This setup consists of a zinc plate anode and a cathode supported by high-entropy spinel ferrite with an electrolyte solution of 6 M KOH + 0.2 M $Zn(OAc)_2$. In rechargeable ZABs, the air cathode plays a pivotal role in both the charging process involving the OER and the discharging process involving the ORR. The overall reactions occurring within the ZABs are represented as follows:

at the air cathode: $O_2 + 2H_2O + 4e^- \leftrightarrow 4OH^-$

at the zinc anode: $Zn + 4OH^- \leftrightarrow Zn(OH)_4^{2-} + 2e^-$

$Zn(OH)_4^{2-} \leftrightarrow ZnO + H_2O + 2OH^-$

overall reaction: $2Zn + O_2 \leftrightarrow 2ZnO$

Both Mg-Fe_2O_4 and Tm-Fe_2O_4 electrocatalyst-based ZABs exhibit similar open-circuit potential (OCP) around 1.56 V. Figure 7a represents the power density and polarization curves of ZABs. Notably, ZAB incorporating Tm-Fe_2O_4 shows a narrower charge−discharge voltage gap compared to its Mg-Fe_2O_4 counterpart. This is highlighted in the polarization curves, which depict a minimized voltage gap during the OER and ORR phases for the Tm-Fe_2O4-based ZAB, which is attributed to its lower BI. This characteristic enhances the rechargeability of the Tm-Fe_2O_4-based ZAB. Furthermore, the cathode featuring Tm-Fe_2O_4 reached a peak power density of 51.72 mW cm^{-2} at an elevated current density of 100 mA cm^{-2}, surpassing the performance of Mg-Fe_2O_4, which achieved a peak power density of 44.95 mW cm^{-2} at 92.90 mA cm^{-2}. Moreover, to understand the electrochemical durability of ZABs, the cyclic charge−discharge longevity of the batteries was measured at a 5 mA cm^{-2} current density. The ZAB featuring a Tm-Fe_2O_4 cathode demonstrated charge and discharge voltages of approximately 2 and 1.15 V, respectively, during cycles, maintaining a voltage gap of 850 mV, as depicted in Figure 7b. Conversely, the ZAB employing an Mg-Fe_2O_4 cathode presented charge and discharge voltages of around 2.2 and 1.1 V, respectively, showcasing a broader voltage gap than that of Tm-Fe_2O_4 during the cyclic charge−discharge processes since Mg-Fe_2O_4 exhibits lower bifunctional electrocatalytic activity. The charge and discharge voltages of the ZAB with both electrocatalysts remain stable for more than 200 h of cyclic test. While the Tm-Fe_2O_4-based ZAB outperformed in terms of peak power density and minimized voltage gap, the Mg-Fe_2O_4-based ZAB also demonstrated commendable stability in battery operation with a slightly higher voltage gap.

4. CONCLUSIONS

In this study, we have successfully synthesized a novel high-entropy spinel ferrite (Mg-Fe_2O_4) utilizing earth-abundant 2+ ions through the facile sol−gel Pechini method. This innovative approach has resulted in the development of Mg-Fe_2O_4 with a cubic spinel structure that aligns closely with its transition metal counterparts (Tm-Fe_2O_4) in terms of lattice constants. Notably, the nontransitional metals at the A-site of the spinel structure do not compromise the integrity of the cubic spinel structure, highlighting the robustness of the synthesized material. In addition to sharing similar crystal structures, the HESFs demonstrate equivalent oxidation behavior, indicating a level of uniformity in their chemical properties. Interestingly, while Tm-Fe_2O_4 shows superior OER and ORR activities due to its lower work function and enhanced O 2p hybridization, the Mg-Fe_2O_4 variant also delivers commendable OER and ORR performance with a comparably low work function value. This suggests that the performance gap between transition-metal-based and more sustainable alternatives is narrowing. Crucially, Mg-Fe_2O_4 exhibits stable battery performance over 200 h, underscoring its potential as a durable material for energy storage applications. This finding is significant, as it demonstrates that the incorporation of cheaper and more abundant materials does not necessitate a tradeoff in performance or longevity. This work signifies a pivotal step forward in the development of HESFs for rechargeable zinc-air batteries. By demonstrating that materials synthesized from earth-abundant elements can exhibit similar structural and electronic characteristics as their transition-metal-containing counterparts, we have expanded the potential for using more accessible and sustainable materials in energy conversion and storage applications. This approach not only broadens the resource base for HESFs but also aligns with sustainability goals by leveraging materials that are more readily available and less environmentally taxing.

■ ASSOCIATED CONTENT

Supporting Information

The Supporting Information is available free of charge at https://pubs.acs.org/doi/10.1021/acsaem.4c01227.

Main XRD peaks of Mg-Fe_2O_4 and Tm-Fe_2O_4 at 30.1 and 35.44°, respectively (TIF)

■ AUTHOR INFORMATION

Corresponding Author

Cigdem Toparli − *Department of Metallurgical and Materials Engineering, Middle East Technical University, Ankara 06800, Turkey;* orcid.org/0000-0002-4374-4910; Email: ctoparli@metu.edu.tr

Authors

Tuncay Erdil − *Department of Metallurgical and Materials Engineering, Middle East Technical University, Ankara 06800, Turkey;* orcid.org/0000-0002-5187-5902

Cagla Ozgur − *Department of Metallurgical and Materials Engineering, Middle East Technical University, Ankara 06800, Turkey*

Uygar Geyikci − *Department of Metallurgical and Materials Engineering, Middle East Technical University, Ankara 06800, Turkey*

Ersu Lokcu − *Department of Metallurgical and Materials Engineering, Eskisehir Osmangazi University, Eskisehir 26040, Turkey;* orcid.org/0000-0002-1972-627X

Complete contact information is available at: https://pubs.acs.org/10.1021/acsaem.4c01227

Notes

The authors declare no competing financial interest.

■ ACKNOWLEDGMENTS

The financial support provided by the Scientific and Technological Research Council of Turkey (TUBITAK) under the grant No: 222M254 is greatly acknowledged.

■ REFERENCES

(1) Nguyen, T. X.; Su, Y.; Lin, C.; Ruan, J.; Ting, J. A New High Entropy Glycerate for High Performance Oxygen Evolution Reaction. *Advanced. Science* **2021**, *8* (6), No. 2002446.
(2) Jin, Z.; Lyu, J.; Zhao, Y.-L.; Li, H.; Lin, X.; Xie, G.; Liu, X.; Kai, J.-J.; Qiu, H.-J. Rugged High-Entropy Alloy Nanowires with in Situ Formed Surface Spinel Oxide As Highly Stable Electrocatalyst in Zn−Air Batteries. *ACS Mater Lett* **2020**, *2* (12), 1698−1706.
(3) Ma, Y.; Ma, Y.; Wang, Q.; Schweidler, S.; Botros, M.; Fu, T.; Hahn, H.; Brezesinski, T.; Breitung, B. High-Entropy Energy Materials: Challenges and New Opportunities. *Energy Environ Sci* **2021**, *14* (5), 2883−2905.
(4) Huo, W.-Y.; Wang, S.-Q.; Zhu, W.-H.; Zhang, Z.-L.; Fang, F.; Xie, Z.-H.; Jiang, J.-Q. Recent Progress on High-Entropy Materials for Electrocatalytic Water Splitting Applications. *Tungsten* **2021**, *3* (2), 161−180.
(5) Sarkar, A.; Wang, Q.; Schiele, A.; Chellali, M. R.; Bhattacharya, S. S.; Wang, D.; Brezesinski, T.; Hahn, H.; Velasco, L.; Breitung, B. High-Entropy Oxides: Fundamental Aspects and Electrochemical Properties. *Adv. Mater.* **2019**, *31* (26), No. 1806236.
(6) Talluri, B.; Yoo, K.; Kim, J. High Entropy Spinel Metal Oxide (CoCrFeMnNi)3O4 Nanoparticles as Novel Efficient Electrocatalyst for Methanol Oxidation and Oxygen Evolution Reactions. *J Environ Chem Eng* **2022**, *10* (1), No. 106932.
(7) Sarkar, A.; Breitung, B.; Hahn, H. High Entropy Oxides: The Role of Entropy, Enthalpy and Synergy. *Scr Mater* **2020**, *187*, 43−48.
(8) Yeh, J.-W.; Lin, S.-J. Breakthrough Applications of High-Entropy Materials. *J. Mater. Res.* **2018**, *33* (19), 3129−3137.
(9) McCormack, S. J.; Navrotsky, A. Thermodynamics of High Entropy Oxides. *Acta Mater* **2021**, *202*, 1−21.
(10) Liu, Z.; Tang, Z.; Song, Y.; Yang, G.; Qian, W.; Yang, M.; Zhu, Y.; Ran, R.; Wang, W.; Zhou, W.; Shao, Z. High-Entropy Perovskite Oxide: A New Opportunity for Developing Highly Active and Durable Air Electrode for Reversible Protonic Ceramic Electrochemical Cells. *Nanomicro Lett* **2022**, *14* (1), 217.
(11) Xu, X.; Shao, Z.; Jiang, S. P. High-Entropy Materials for Water Electrolysis. *Energy Technology* **2022**, *10* (11), No. 2200573.
(12) Katzbaer, R. R.; dos Santos Vieira, F. M.; Dabo, I.; Mao, Z.; Schaak, R. E. Band Gap Narrowing in a High-Entropy Spinel Oxide Semiconductor for Enhanced Oxygen Evolution Catalysis. *J. Am. Chem. Soc.* **2023**, *145* (12), 6753−6761.
(13) Kante, M. V.; Weber, M. L.; Ni, S.; van den Bosch, I. C. G.; van der Minne, E.; Heymann, L.; Falling, L. J.; Gauquelin, N.; Tsvetanova, M.; Cunha, D. M.; Koster, G.; Gunkel, F.; Nemšák, S.; Hahn, H.; Velasco Estrada, L.; Baeumer, C. A High-Entropy Oxide as High-Activity Electrocatalyst for Water Oxidation. *ACS Nano* **2023**, *17* (6), 5329−5339.
(14) Abdelhafiz, A.; Tanvir, A. N. M.; Zeng, M.; Wang, B.; Ren, Z.; Harutyunyan, A. R.; Zhang, Y.; Li, J. Pulsed Light Synthesis of High Entropy Nanocatalysts with Enhanced Catalytic Activity and Prolonged Stability for Oxygen Evolution Reaction. *Advanced. Science* **2023**, *10* (18), No. 2300426.
(15) Ozgur, C.; Erdil, T.; Geyikci, U.; Okuyucu, C.; Lokcu, E.; Kalay, Y. E.; Toparli, C. Engineering Oxygen Vacancies in $(FeCrCoMnZn)_3O_{4-\delta}$ High Entropy Spinel Oxides Through Altering Fabrication Atmosphere for High-Performance Rechargeable Zinc-Air Batteries. *Global. Challenges* **2024**, *8* (1), No. 2300199.
(16) Erdil, T.; Toparli, C. B-Site Effect on High-Entropy Perovskite Oxide as a Bifunctional Electrocatalyst for Rechargeable Zinc−Air Batteries. *ACS Appl Energy Mater* **2023**, *6* (21), 11255−11267.
(17) Einert, M.; Waheed, A.; Lauterbach, S.; Mellin, M.; Rohnke, M.; Wagner, L. Q.; Gallenberger, J.; Tian, C.; Smarsly, B. M.; Jaegermann, W.; Hess, F.; Schlaad, H.; Hofmann, J. P. Sol-Gel-Derived Ordered Mesoporous High Entropy Spinel ferrites and Assessment of Their Photoelectrochemical and Electrocatalytic Water Splitting Performance. *Small* **2023**, *19* (14), No. 2205412.
(18) Zander, J.; Wölfel, J. P.; Weiss, M.; Jiang, Y.; Cheng, N.; Zhang, S.; Marschall, R. Medium- and High-Entropy Spinel Ferrite Nanoparticles via Low-Temperature Synthesis for the Oxygen Evolution Reaction. *Adv Funct Mater* **2024**, *34* (4), No. 2310179.
(19) Zhang, Y.; Dai, W.; Zhang, P.; Lu, T.; Pan, Y. In-Situ Electrochemical Tuning of (CoNiMnZnFe)3O3.2 High-Entropy Oxide for Efficient Oxygen Evolution Reactions. *J. Alloys Compd.* **2021**, *868*, No. 159064.
(20) Gu, Y.; Bao, A.; Wang, X.; Chen, Y.; Dong, L.; Liu, X.; Pan, H.; Li, Y.; Qi, X. Engineering the Oxygen Vacancies of Rocksalt-Type High-Entropy Oxides for Enhanced Electrocatalysis. *Nanoscale* **2022**, *14* (2), 515−524.
(21) Cherevko, S.; Geiger, S.; Kasian, O.; Kulyk, N.; Grote, J.-P.; Savan, A.; Shrestha, B. R.; Merzlikin, S.; Breitbach, B.; Ludwig, A.; Mayrhofer, K. J. J. Oxygen and Hydrogen Evolution Reactions on Ru, RuO 2, Ir, and IrO 2 Thin Film Electrodes in Acidic and Alkaline Electrolytes: A Comparative Study on Activity and Stability. *Catal. Today* **2016**, *262*, 170−180.
(22) Sarkar, A.; Velasco, L.; Wang, D.; Wang, Q.; Talasila, G.; de Biasi, L.; Kübel, C.; Brezesinski, T.; Bhattacharya, S. S.; Hahn, H.; Breitung, B. High Entropy Oxides for Reversible Energy Storage. *Nat Commun* **2018**, *9* (1), 3400.
(23) Wang, D.; Jiang, S.; Duan, C.; Mao, J.; Dong, Y.; Dong, K.; Wang, Z.; Luo, S.; Liu, Y.; Qi, X. Spinel-Structured High Entropy Oxide (FeCoNiCrMn)3O4 as Anode towards Superior Lithium Storage Performance. *J. Alloys Compd.* **2020**, *844*, No. 156158.
(24) Nguyen, T. X.; Tsai, C.-C.; Patra, J.; Clemens, O.; Chang, J.-K.; Ting, J.-M. Co-Free High Entropy Spinel Oxide Anode with Controlled Morphology and Crystallinity for Outstanding Charge/Discharge Performance in Lithium-Ion Batteries. *Chemical Engineering Journal* **2022**, *430*, No. 132658.
(25) Bayraktar, D. O.; Lökçü, E.; Ozgur, C.; Erdil, T.; Toparli, C. Effect of Synthesis Environment on the Electrochemical Properties of (<scp > FeMnCrCoZn</Scp>) < scp> $_3$ O $_4$ < /Scp> High-entropy Oxides for Li-ion Batteries. *Int. J. Energy Res.* **2022**, *46* (15), 22124−22133.
(26) Sanchez-Lievanos, K. R.; Stair, J. L.; Knowles, K. E. Cation Distribution in Spinel Ferrite Nanocrystals: Characterization, Impact on Their Physical Properties, and Opportunities for Synthetic Control. *Inorg Chem* **2021**, *60* (7), 4291−4305.
(27) Mao, A.; Xiang, H.-Z.; Zhang, Z.-G.; Kuramoto, K.; Zhang, H.; Jia, Y. A New Class of Spinel High-Entropy Oxides with Controllable Magnetic Properties. *J Magn Magn Mater* **2020**, *497*, No. 165884.
(28) Harada, M.; Kotegawa, F.; Kuwa, M. Structural Changes of Spinel MCo $_2$ O $_4$ (M = Mn, Fe, Co, Ni, and Zn) Electrocatalysts during the Oxygen Evolution Reaction Investigated by In Situ X-Ray Absorption Spectroscopy. *ACS Appl Energy Mater* **2022**, *5* (1), 278−294.
(29) Wang, X.; Ouyang, T.; Wang, L.; Zhong, J.; Liu, Z. Surface Reorganization on Electrochemically-Induced Zn−Ni−Co Spinel Oxides for Enhanced Oxygen Electrocatalysis. *Angew. Chem.* **2020**, *132* (16), 6554−6561.
(30) Liu, X.-M.; Cui, X.; Dastafkan, K.; Wang, H.-F.; Tang, C.; Zhao, C.; Chen, A.; He, C.; Han, M.; Zhang, Q. Recent Advances in Spinel-Type Electrocatalysts for Bifunctional Oxygen Reduction and Oxygen Evolution Reactions. *Journal of Energy Chemistry* **2021**, *53*, 290−302.
(31) Ferreira, L. S.; Silva, T. R.; Silva, V. D.; Raimundo, R. A.; Simões, T. A.; Loureiro, F. J. A.; Fagg, D. P.; Morales, M. A.; Macedo, D. A. Spinel Ferrite MFe2O4 (M = Ni, Co, or Cu) Nanoparticles Prepared by a Proteic Sol-Gel Route for Oxygen Evolution Reaction. *Advanced Powder Technology* **2022**, *33* (1), No. 103391.
(32) González-Flores, D.; Klingan, K.; Chernev, P.; Loos, S.; Mohammadi, M. R.; Pasquini, C.; Kubella, P.; Zaharieva, I.; Smith, R.

https://doi.org/10.1021/acsaem.4c01227
ACS Appl. Energy Mater. 2024, 7, 7775−7786

D. L.; Dau, H. Nickel-Iron Catalysts for Electrochemical Water Oxidation − Redox Synergism Investigated by *in Situ* X-Ray Spectroscopy with Millisecond Time Resolution. *Sustain Energy Fuels* **2018**, *2* (9), 1986−1994.
(33) Qin, H.; He, Y.; Xu, P.; Huang, D.; Wang, Z.; Wang, H.; Wang, Z.; Zhao, Y.; Tian, Q.; Wang, C. Spinel ferrites (MFe2O4): Synthesis, Improvement and Catalytic Application in Environment and Energy Field. *Adv. Colloid Interface Sci.* **2021**, *294*, No. 102486.
(34) Roger, I.; Shipman, M. A.; Symes, M. D. Earth-Abundant Catalysts for Electrochemical and Photoelectrochemical Water Splitting. *Nat Rev Chem* **2017**, *1* (1), No. 0003.
(35) Simon, C.; Timm, J.; Tetzlaff, D.; Jungmann, J.; Apfel, U.; Marschall, R. Mesoporous $NiFe_2O_4$ with Tunable Pore Morphology for Electrocatalytic Water Oxidation. *ChemElectroChem* **2021**, *8* (1), 227−239.
(36) Simon, C.; Zakaria, M. B.; Kurz, H.; Tetzlaff, D.; Blösser, A.; Weiss, M.; Timm, J.; Weber, B.; Apfel, U.; Marschall, R. Magnetic $NiFe_2O_4$ Nanoparticles Prepared via Non-Aqueous Microwave-Assisted Synthesis for Application in Electrocatalytic Water Oxidation. *Chem. − Eur. J.* **2021**, *27* (68), 16990−17001.
(37) Zhu, S.; Lei, J.; Qin, Y.; Zhang, L.; Lu, L. Spinel Oxide $CoFe_2O_4$ Grown on Ni Foam as an Efficient Electrocatalyst for Oxygen Evolution Reaction. *RSC Adv* **2019**, *9* (23), 13269−13274.
(38) Tian, L.; Zhang, Z.; Liu, S.; Li, G.; Gao, X. High-Entropy Spinel Oxide Nanofibers as Catalytic Sulfur Hosts Promise the High Gravimetric and Volumetric Capacities for Lithium−Sulfur Batteries. *ENERGY & ENVIRONMENTAL MATERIALS* **2022**, *5* (2), 645−654.
(39) Tian, K.-H.; Duan, C.-Q.; Ma, Q.; Li, X.-L.; Wang, Z.-Y.; Sun, H.-Y.; Luo, S.-H.; Wang, D.; Liu, Y.-G. High-Entropy Chemistry Stabilizing Spinel Oxide (CoNiZnXMnLi)3O4 (X = Fe, Cr) for High-Performance Anode of Li-Ion Batteries. *Rare Metals* **2022**, *41* (4), 1265−1275.
(40) Ai, J.; Shuai, Y.; Hu, M.; Cheng, L.; Luo, S.; Li, W.; Chen, Z.; Hu, L.; Zhou, Z. Microstructural Evolution and Catalytic Properties of Novel High-Entropy Spinel ferrites MFe2O4 (M= Mg, Co, Ni, Cu, Zn). *Ceram. Int.* **2023**, *49* (14), 22941−22951.
(41) Sharma, Y.; Mazza, A. R.; Musico, B. L.; Skoropata, E.; Nepal, R.; Jin, R.; Ievlev, A. V.; Collins, L.; Gai, Z.; Chen, A.; Brahlek, M.; Keppens, V.; Ward, T. Z. Magnetic Texture in Insulating Single Crystal High Entropy Oxide Spinel Films. *ACS Appl Mater Interfaces* **2021**, *13* (15), 17971−17977.
(42) Ma, J.; Zhao, B.; Xiang, H.; Dai, F.-Z.; Liu, Y.; Zhang, R.; Zhou, Y. High-Entropy Spinel ferrites MFe2O4 (M = Mg, Mn, Fe, Co, Ni, Cu, Zn) with Tunable Electromagnetic Properties and Strong Microwave Absorption. *Journal of Advanced Ceramics* **2022**, *11* (5), 754−768.
(43) Mansour, A. N.; Brizzolara, R. A. Characterization of the Surface of γ-Fe2O3 Powder by XPS. *Surface Science Spectra* **1996**, *4* (4), 351−356.
(44) Reitz, C.; Suchomski, C.; Haetge, J.; Leichtweiss, T.; Jagličić, Z.; Djerdj, I.; Brezesinski, T. Soft-Templating Synthesis of Mesoporous Magnetic CuFe2O4 Thin Films with Ordered 3D Honeycomb Structure and Partially Inverted Nanocrystalline Spinel Domains. *Chemical Communications* **2012**, *48* (37), 4471.
(45) Penke, Y. K.; Anantharaman, G.; Ramkumar, J.; Kar, K. K. Aluminum Substituted Cobalt Ferrite (Co−Al−Fe) Nano Adsorbent for Arsenic Adsorption in Aqueous Systems and Detailed Redox Behavior Study with XPS. *ACS Appl Mater Interfaces* **2017**, *9* (13), 11587−11598.
(46) Lu, Y.-T.; Chien, Y.-J.; Liu, C.-F.; You, T.-H.; Hu, C.-C. Active Site-Engineered Bifunctional Electrocatalysts of Ternary Spinel Oxides, $M_{0.1}Ni_{0.9}Co_2O_4$ (M: Mn, Fe, Cu, Zn) for the Air Electrode of Rechargeable Zinc−Air Batteries. *J. Mater. Chem. A* **2017**, *5* (39), 21016−21026.
(47) Saravanakumar, T.; Sathiya Bama, S.; Selvaraju, T.; Sardhar Basha, S. J. Hexacyanoferrate-Complex-Derived $NiFe_2O_4/CoFe_2O_4$ Heterostructure−MWCNTs for an Efficient Oxygen Evolution Reaction. *Energy & Fuels* **2021**, *35* (6), 5372−5382.
(48) Wang, D.; Liu, Z.; Du, S.; Zhang, Y.; Li, H.; Xiao, Z.; Chen, W.; Chen, R.; Wang, Y.; Zou, Y.; Wang, S. Low-Temperature Synthesis of Small-Sized High-Entropy Oxides for Water Oxidation. *J Mater Chem A Mater* **2019**, *7* (42), 24211−24216.
(49) Erdil, T.; Lokcu, E.; Yildiz, I.; Okuyucu, C.; Kalay, Y. E.; Toparli, C. Facile Synthesis and Origin of Enhanced Electrochemical Oxygen Evolution Reaction Performance of 2H-Hexagonal $Ba_2CoMnO_{6-\delta}$ as a New Member in Double Perovskite Oxides. *ACS Omega* **2022**, *7* (48), 44147−44155.
(50) Lökçü, E.; Toparli, Ç.; Anik, M. Electrochemical Performance of $(MgCoNiZn)_{1-x}Li_xO$ High-Entropy Oxides in Lithium-Ion Batteries. *ACS Appl Mater Interfaces* **2020**, *12* (21), 23860−23866.
(51) Yuan, R.; Bi, W.; Zhou, T.; Zhang, N.; Zhong, C.; Chu, W.; Yan, W.; Xu, Q.; Wu, C.; Xie, Y. Two-Dimensional Hierarchical Fe−N−C Electrocatalyst for Zn-Air Batteries with Ultrahigh Specific Capacity. *ACS Mater Lett* **2020**, *2* (1), 35−41.
(52) Alegre, C.; Modica, E.; Aricò, A. S.; Baglio, V. Bifunctional Oxygen Electrode Based on a Perovskite/Carbon Composite for Electrochemical Devices. *J. Electroanal. Chem.* **2018**, *808*, 412−419.
(53) Wang, F.; Borodin, O.; Gao, T.; Fan, X.; Sun, W.; Han, F.; Faraone, A.; Dura, J. A.; Xu, K.; Wang, C. Highly Reversible Zinc Metal Anode for Aqueous Batteries. *Nat. Mater.* **2018**, *17* (6), 543−549.

NOTE ADDED AFTER ASAP PUBLICATION

The version of this paper that was published ASAP September 10, 2024, was missing the correct abstract graphic. The corrected version was reposted September 12, 2024.

https://doi.org/10.1021/acsaem.4c01227
ACS Appl. Energy Mater. 2024, 7, 7775−7786